Large area defrosting windows based on electrothermal heating of highly conducting and transmitting Ag wire mesh†

S. Kiruthika, Ritu Gupta‡ and Giridhar U. Kulkarni*

Highly interconnected crackles were obtained by spreading commercially available low cost crackle wall paint based precursor by the drop coating technique. An interconnected Ag mesh was fabricated by depositing metal over the crackle network followed by the removal of the template. The metal network is well conducting (1 Ω $\square^{-1}$) with transmittance of ~77% over the fabricated area, 18×15 cm^2. By joule heating using few volts, uniform temperatures up to 170 °C were achieved on the electrode area and a high thermal resistance of 255.2 °C cm^2 W^{-1} was obtained. The electrode was tested for defrosting application by exposing it to liquid nitrogen (LN$_2$) vapors at ~-60 °C while applying 8.5 V for 2 min, when the frost disappeared making the display board below, visible. The transparent heater could successfully withstand an ultrasonication test, as well as many defrosting cycles.

Introduction

The changes in the climatic condition often result in frosting and icing that severely affect human life, especially in cold countries.[1] Frost formation and icing pose serious safety issues for aircrafts, telecommunication and road safety signals by blocking the displays, and thus leading to traffic failure and severe accidents.[2,3] Therefore, increasing efforts have been made towards designing anti-icing and defrosting surfaces by texturing, chemical coatings *etc.*[4,5] The patterning and structuring of a surface is usually performed to mimic lotus and rice leaf type nanostructures.[6,7] However, these methods need optimization in terms of processing and scalability for practical applications. The superhydrophobic chemical coatings, such as polymers and their nanocomposites, are used to prevent frost formation; however, not all superhydrophobic surfaces are icephobic in nature.[7,8] In this context, electrothermal or joule heating is considered to be one of the most efficient approaches.[9] The de-icing of conducting transmission lines by joule heating is universally adopted. Similarly, printed metal

grids are highly efficient for defrosting applications, but being visibly thick they obstruct ~50% of the total view, which is certainly undesired.[10] Several devices, such as outdoor displays, avionic displays, automobile windows, as well in periscopes, require clear visibility irrespective of the weather conditions, and thus the development of visibly transparent heaters is a necessity.[11,12]

Transparent conducting oxide, tin doped indium oxide (ITO) has been the obvious choice as heating element because of its proven performance in optoelectronics, namely high transmittance in the visible region, low sheet resistance and stability in environmental conditions.[13–15] However, due to indium scarcity and the associated cost, ITO is considered prohibitive, particularly in large area applications.[16–18] Moreover, high power consumption and slow thermal response associated with ITO based heaters have limited its usage. With major developments in optoelectronics in the last two decades, new alternative transparent conductors, such as graphene,[19] carbon nanotube (CNT) network,[20,21] metal nanowire,[22,23] metal mesh network,[24] PEDOT,[25] as well as hybrid films,[26–28] have been developed and there has been an increasing interest in using these non-ITO based alternatives in electrothermal applications. Thus, recently, attempts have been made to fabricate transparent heaters with graphene,[11,29–31] CNT,[12,32–36] nanocrystalline diamond,[37] metallic nanowires,[38] and sometimes involving their hybrids.[39] CNT and graphene based heaters have shown excellent heating performance with uniform heat distribution although the operating voltage and the power required for their operation are usually high,[11,29,35] as in general, they possess high sheet resistance. A good heater should give uniform thermal distribution over the heating area and achieve higher temperatures with low power. Highly conducting metal

Chemistry & Physics of Materials Unit and Thematic Unit of Excellence in Nanochemistry, Jawaharlal Nehru Centre for Advanced Scientific Research, Jakkur P.O., Bangalore 560 064, India. E-mail: kulkarni@jncasr.ac.in

‡ Present address: Birck Nanotechnology Centre, Purdue University, West Lafayette, Indiana-47907, USA.

nanostructures, on the other hand, can work with lower operating voltages with better response time, but the nanowire junctions are prone to oxidation and failure at temperatures typically above 50 °C.[22] To improve the junction resistance, and thus the overall performance of the heater, several post-synthesis treatment and hybrid structuring methods have been reported.[38] While these remedies may bring down the sheet resistance to suit optoelectronic applications (typically few Ω $\square^{-1}$), the overall resistance for a large area can be still high (a few tens or hundreds of Ω) requiring high power for electro-thermal applications.[41] Further, the well-known trade-off between transmittance and sheet resistance in a transparent conductor is an added constraint.[39,40] Sheet resistance cannot be easily lowered without sacrificing the transmittance even with new generation alternatives. Extremely low sheet resistance ($\sim 1 \Omega \square^{-1}$) attained without disturbing transmittance is highly desirable, which is rather challenging.

The fabrication of transparent electrodes using template based methods is becoming demanding.[40–42] Recently, we have developed a crackle templating method of fabricating metal wire networks devoid of crossbar junctions and shown that their performance parameters are close to those of ITO.[43–46] In this templating method, the wire thickness could be increased to lower the sheet resistance without disturbing transmittance. Because of low resistance, the wire mesh could be employed as a joule heater to reach annealing temperatures of a few hundred degrees Celsius over cm^2 areas.[43] In this study, we examine their efficacy as transparent heaters, especially in the context of defrosting over a large area. For this purpose, we have explored a simpler template formation method, unlike before, involving only a dropper or a brush, which requires minimal effort and no instrumentation. In this manner, the fabrication should be scalable to large areas with only a linear increase in cost. The prepared Ag mesh based transparent heaters have shown stability in defrosting even at sub-zero temperatures.

Results and discussion

Coating of the crackle template deserves some detailed mention. In our earlier study,[45] the crackle precursor, a colloidal dispersion of SiO$_2$ nanoparticles (see ESI, Fig. S1†), was spread over A4 sized substrates by the rod coating method to obtain the crackle template. Here in this study, the precursor after some optimisation is examined for its ability to extend over even larger areas by a simple drop coating technique, which does not require any instrumentation or infrastructure. The primary requirement for drop coating a precursor is that the drops should effortlessly merge to form a uniformly thick wet layer all over. The uniformity in the layer thickness is important as it determines the properties of the crack network,[47,48] namely the crack width, crack spacing, interconnectivity. In order to examine this aspect, two drops of the crackle precursor were closely positioned, but separated (Fig. 1a). As the precursor wets the glass substrate with low contact angle (inset of Fig. 1a), the drops gradually spread and merge to form a dumbbell shaped layer as drying sets in. Optical profiler images from the different marked regions (see Fig. 1b) show cracks of similar widths
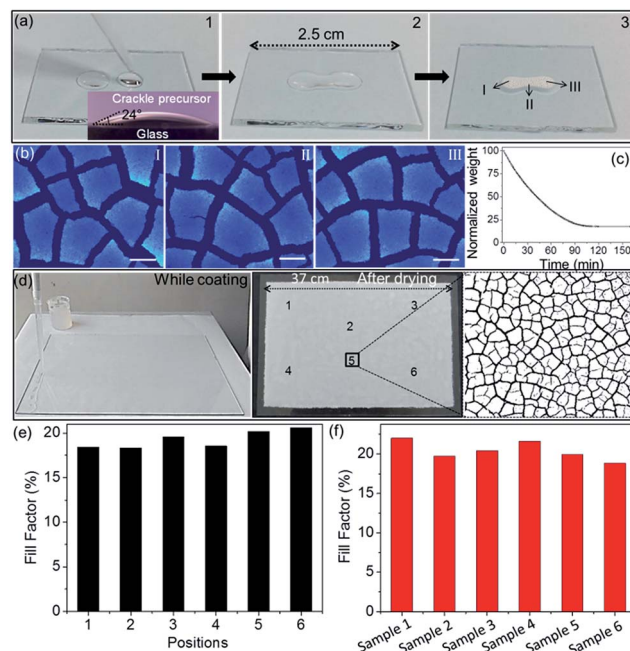

Fig. 1 (a) Shows spreading of the two drops of the crackle precursor leading to a uniform film. Inset is the contact angle measured between crackle precursor and glass substrate. The completely dried and crackled film was obtained after 20 min. (b) The optical profiler images taken at areas marked in (a) are shown in I, II and III. Scale bar is 200 µm and thickness of the crackle precursor is ~75 µm. (c) Change in the weight of the crackle precursor coated on glass substrate versus time. Images taken (d) while drop coating crackle precursor over a 37 × 25 cm^2 area glass substrate and after drying leading to crackle network formation. Fill factor of crackle network (the black trace refers to crackle network and white region corresponds to crackle precursor) from marked region in dried film and (e) histogram of fill factor calculated from different positions of sample shown in (d). (f) The histogram representation of fill factor calculated from six samples.

indicating uniform thickness of the precursor layer. The drying process is rather slow (Fig. 1c), which is clearly an advantage for extending drop coating to large areas. Under optimized conditions (ESI, Fig. S2†), the crackle precursor was drop coated over a big glass substrate as shown in Fig. 1d (also see ESI, Fig. S3†), which upon drying in air produced a crackle network shown in Fig. 1d and ESI S4a.† A magnified view of an SEM image (ESI, Fig. S4b†) shows ~40–50 µm wide crackles that are deep down to the substrate except few little left over precursor in the grooves. The uniformity of the crackle network formed over large area glass substrate was evidenced from the fill factor analysis performed from various locations (see Fig. 1d and ESI S5†). From the histogram shown in Fig. 1e, the fill factor of the network (black regions) is found to be nearly 20% from various locations, which is easily reproducible over many samples (Fig. 1f and ESI S6†). As is done during wall painting, a brush can aid to evenly spread the drying layer over ultra large areas (ESI, Fig. S7†).

Following Ag deposition by a physical evaporation method, the template layer was washed away in acetone leaving behind Ag mesh on the substrate (see schematic). The optical image in Fig. 2a shows interconnected Ag wires in the network with ~300
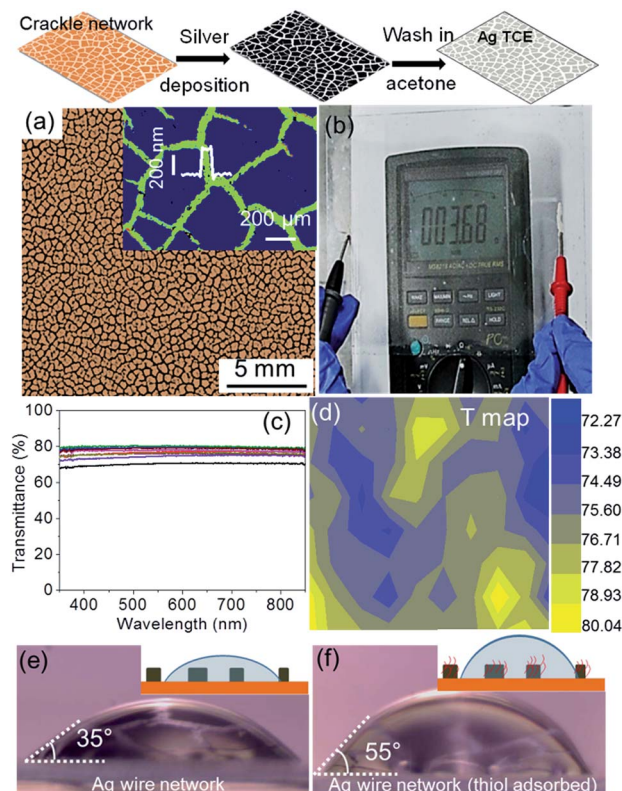
Fig. 2 Schematic for TCE fabrication is shown. (a) Optical image of the Ag mesh on glass. Inset is the optical profiler image (thickness ~300 nm). (b) The image of the transparent conductor connected to a multimeter. (c) Transmittance spectra measured from 10 different locations and (d) the transmittance map. The bright yellow and blue coloured regions correspond to 80% and 72% transmittance, respectively, with other intermediate colours representing transmittance in between 80% to 72%. Contact angle of water on Ag mesh/glass, (e) before and (f) after coating with 1-hexadecanethiol. The wire network is seen in reflection within the drop. Insets are schematic representations.

nm thickness, as measured using an optical profiler (inset in Fig. 2a). A SEM image and EDS mapping of the Ag mesh (ESI, Fig. S8†) show continuous Ag signal in the form of an interconnected junctionless wire with only slight defects because of the unwashed crack precursor. This crackle templating method is scalable as seen with the network formed over 18×15 cm^2 area. A two probe measurement across 18 cm using a multimeter showed resistance of 3.68 Ω (Fig. 2b). The sheet resistance of Ag mesh is ~1 Ω $\square^{-1}$. Obviously, such low sheet resistance is achieved because of seamless junctions and high thickness (300 nm) of the mesh.

The transmittance spectra measured from 10 different regions of the network are shown in Fig. 2c and an average transmittance value of ~77% ± 2.1% was obtained over the entire spectrum (see ESI, Fig. S9†). A typical transmission map over a 2.5×2.5 cm^2 area is shown in Fig. 2d. This value of transmittance is commendable given the low sheet resistance value. Thus, with this mesh structure, one can lower the resistance by increasing the thickness without affecting the transmittance. From transmittance and sheet resistance values, the

figure of merit (FoM, σ_{DC}/σ_{OP}) was estimated for the transparent conductor, using the eqn (1)[10]

$$\sigma_{DC}/\sigma_{OP} = Z_o/2R_s(T^{-1/2} - 1) \qquad (1)$$

The estimated FoM value is 1350, which is significant when compared to literature values.[42] Further, the surface property of the metal mesh can be exploited by chemically modifying it. By adsorbing a monolayer of 1-hexadecanethiol on the Ag mesh surface, the water contact angle was enhanced from 35° (Fig. 2e) to ~55° (Fig. 2f).[49] Higher contact angle is beneficial in self-cleaning of the transparent electrode.

The performance of the Ag mesh as a transparent defrosting panel is demonstrated by joule-heating it under frosting conditions. First, the frost was allowed to form on the glass panel by placing it over a liquid nitrogen (LN$_2$) container. The panel appeared opaque as its temperature dropped to ~−60 °C (measured using a thermocouple) because of the frost formation (Fig. 3a).

Upon applying 8.5 V to the end terminals made of Ag epoxy, the frost began to melt leading to a clear view in ~2 min even in the presence of LN$_2$ vapors (Fig. 3b and c and ESI, Movie 1† (speed, 6×)). A clear view of the display board from beneath was possible following defrosting (see bottom images in Fig. 3). To the best of our knowledge, defrosting from such low temperatures has not been reported hitherto. Most literature results pertain to near zero degrees Celsius (see Table 1). Importantly, in this study, the transparent heater was tested while it was kept in frosting conditions just like the real-life application. Other notable point is that it works at nominal power/voltage (see Table 1), because of its low sheet resistance. The water droplets retaining over the Ag mesh could be avoided by holding the display board in vertical position rather than horizontal. Further, by coating with thiol molecules, the contact angle can be increased to assist the water removal.

In the literature, defrosting transparent heaters have been fabricated using carbon derivatives (CNTs,[12,33,34] graphene oxide (GO),[11,50] graphene[31]), Ag nanowires,[38,51] composites of GO and Ag nanowires[52] and ITO.[14,15] Carbon based heaters with typically high sheet resistances require higher power to melt the frost,[11,31]
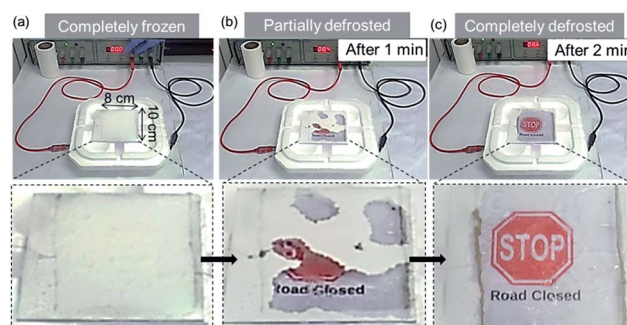

Fig. 3 Performance of Ag mesh/glass as defrosting window panel. (a) Transparent electrode was allowed to freeze by placing it over the LN$_2$ container. (b) After applying 8.5 V for 1 min, the bottom display board was partially visible, and at 2 min (c) the view becomes completely clear.

Table 1 Literature comparison of TCE parameters, maximum temperature achieved, area of the heater, applied voltages and defrosting response time (NA – not available from manuscript)

| Material | TCE | | Temperature achieved (°C) | Area (cm^2) | Frost creating conditions | Voltage (V) | Time (s) | Reference number |
	T (%)	R_s ($\Omega\ \square^{-1}$)						
SWCNT	91.3	1190	120	2.5 × 2.5	Freezer	12	60	12
MWCNT	85	699	37	2.5 × 2.1	Freezer	10	18	33
MWCNT	50	172	42	NA	Freezer	10	10	34
RGO	45	5370	NA	NA	Freezer	10	80	50
RGO	81	6079	45	2 × 1.4	Freezer	60	120	11
Graphene	85	750	55	NA	Freezer	30	30	31
Ag nanowires	92	11	NA	2.5 × 2.5	Freezer	10	40	51
Ag nanowires	>90	50	70	NA	Freezer	12	60	38
RGO/Ag nanowire hybrid	80	27	150	2.5 × 2.5	Freezer	10	40	52
ITO NPs	>90	2500	180	NA	Dry-ice	50	10	15
ITO NPs	>90	633	163	NA	Dry-ice	20	10	14
Patterned Ag	60–80	2	100	6 × 6	Freezer	0.8	>30	10
Ag mesh	77	1	170	10 × 8	−60 °C, LN$_2$ vapors	8.5	120	Present study

compared to the results shown above. Ag nanowire based heaters, although exhibiting lower sheet resistance and operating at relatively lower voltages,[38,52] their outdoor stability is rather poor because of innumerable wire junctions. Zhang et al. used large sized graphene microsheets as protective layer for Ag nanowires.[52] Moreover, in most literature examples,[11,12,31,33,34,38,50–52] the frost load on the heater is nominal with common refrigerator temperatures (∼−5 °C). Often, the frost load is taken off prior to heating, which makes it difficult to assess the efficacy of the heater. ITO based heaters; however, have been demonstrated live in dry ice conditions.[14,15] As evident, we have addressed these issues in the present study. Other advantage of the present method is that the thickness of the metal mesh can be tuned to enhance the performance of defrosting action as shown below.

The electrothermal performance of the Ag mesh/glass was quantitatively examined in detail using IR imaging under ambient conditions (Fig. 4 and ESI, S10†). By applying a DC voltage across the two Ag epoxy contact pads, the mesh was heated and from the IR images the surface temperature was derived. The surface temperature was found to gradually increase to reach a steady state value, which increased with applied voltage. A thermal image obtained with 9 V (see inset of Fig. 4a) shows the temperature distribution in the heater area. The temperature uniformity as seen from the back of the glass substrate could have been better if a thinner substrate was used (in the present study, 1.5 mm). The edges of the substrate however, show lower temperatures because of radiative dissipation. Leaving the contact lines and the edges, the active area as marked in inset of Fig. 4a shows 128 ± 43.5 °C (see marked rectangular region and ESI, Fig. S10c†), which can be improved by reducing substrate thickness and also by defining the electrodes all around. With increase in input voltage from 3 to 9 V, the temperature rise became as steep as shown in Fig. 4a. The response times can be further improved by the above considerations. The steady state temperature of the heater is found to linearly vary with applied power, as shown in Fig. 4b. The slope

of this plot, which represents the thermal resistance of the heater, is estimated to be 255.2 °C cm^2 W^{-1}. Greater the thermal resistance value, superior is the performance of the heater. This value is indeed appreciable; for example, it is 53% higher than SWCNT based heaters.[35] The thermal resistance value does
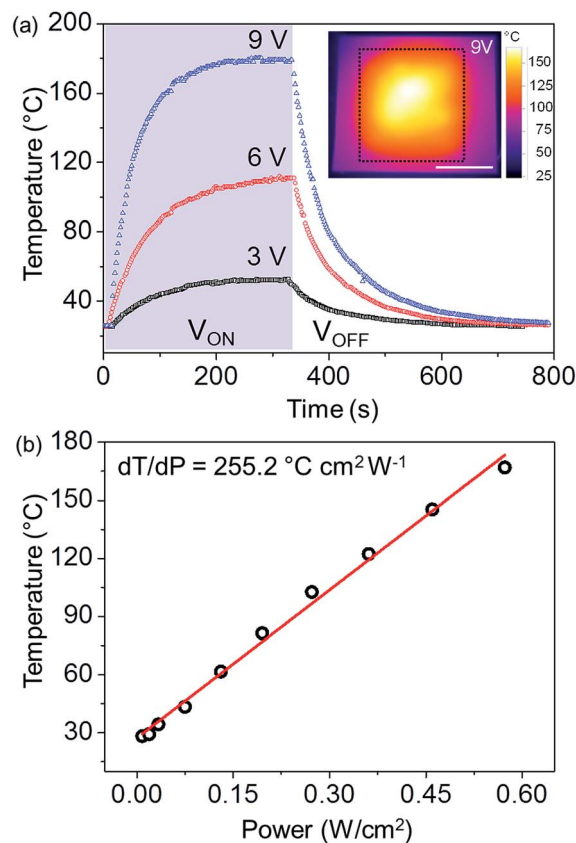
Fig. 4 Performance of Ag mesh/glass based transparent heater. (a) Temperature rise and fall curves for different applied voltages. Inset is the thermal image collected from backside of the TCE at 9 V. Scale bar is 1 cm. (b) Temperature *versus* power plot for the transparent heater.

depend on the mesh thickness; higher thickness will result in lower resistance of the heater; however, the thermal mass will increase.[43] Moderate thicknesses (~100 nm) exhibit high thermal resistance values favouring defrosting action.

The reliability of our Ag mesh based defrosting window panel was examined by performing many frost cycles. The electrode (2.5×2 cm^2) was placed over a LN$_2$ container and allowed to form a thick frost (see ESI, Fig. S11†). By applying 3 V for 60 s, the frost could be melted altogether to provide a clear view. The temperature of the electrode was measured using an IR camera. Once the frost disappeared, the voltage was turned off until a thick frost layer developed again. The electrode was tested for 5 cycles of frost-defrost conditions (see Fig. 5 and ESI, S11†) and the performance were nearly reproducible. It may be noted that this test was performed without any encapsulation. After 6 h of exposure to LN$_2$ vapors and frost conditions and warming to room temperature, the Ag mesh showed no signs of change as determined by XRD (ESI, Fig. S12†).

The practical applicability of the electrodes is further established by examining the robustness of the electrodes. To mimic harsh weather conditions, a Ag mesh/glass electrode was immersed in an ultrasonic water bath (30 kHz), while the resistance was continuously recorded (Fig. 6a). The mesh was hardly affected because of sonication (see Fig. 6b and c and ESI, Movie 2†). As shown in Fig. 6d, the resistance change in the bath was irregular, but within 6%, which may have been because of the contribution from the electronic noise from the sonicator. As soon as sonication was turned off, the resistance reverted back to the normal value. Ag mesh adhesion on glass may be further enhanced by first depositing a few nm thick Ti/Cr layer prior to Ag, as it is conventionally done for thin films. Encapsulation is also expected to enhance its stability and make it scratch resistant.
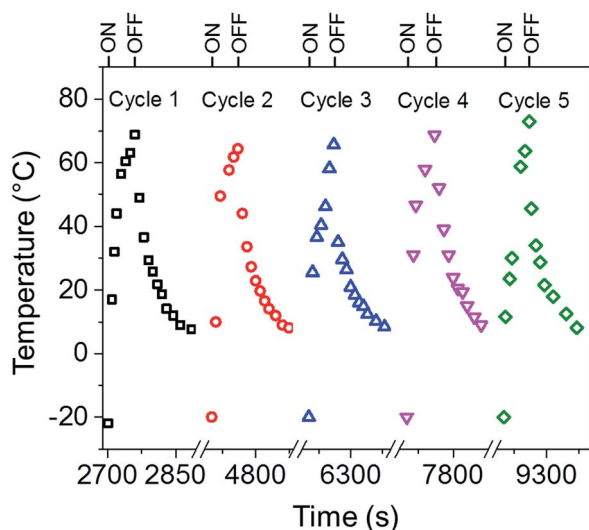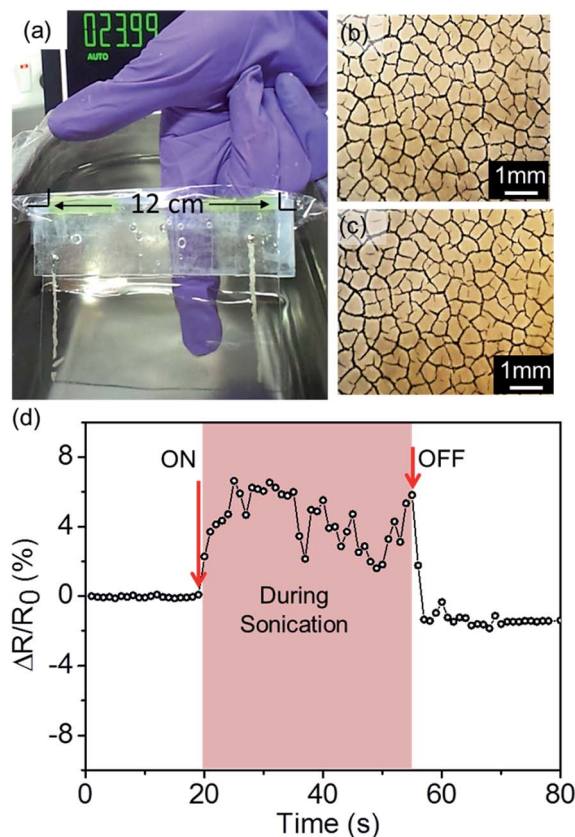

Fig. 6 Robustness of the Ag mesh on glass. (a) Image showing the ultrasonication set up to test the adhesion of the Ag mesh electrode. Optical microscope images of the fabricated Ag electrode (b) before and (c) after ultrasonication test. (d) Relative variation in resistance with time recorded during ultrasonication test.

Conclusions

In this study, we have fabricated transparent conducting electrodes by depositing metal (Ag) over spontaneously formed crackle network as a template made using commercially available crackle paint. The template was produced by a simple drop coating technique. Importantly, no external heating or power input was required; therefore, the method is suitable for low cost production. Thus, formed electrode is highly conducting (1 Ω □$^{-1}$) over a large area with transmittance of ~77% which was used as a transparent heater. The thermal performance of the heater was examined by applying different voltages and a high thermal resistance of 255.2 °C cm^2 W^{-1} was obtained. The efficacy of the transparent heater (10×8 cm^2) was demonstrated by conducting a defrosting experiment, wherein the frost formed by exposing to LN$_2$ vapors could be completely removed by joule heating at 8.5 V for 2 min. Thus, the fabricated electrodes can be used in practical applications as defrosting window panels even when the external temperature is close to polar temperatures (−60 °C). The power required is nominal. The heater is highly robust as evidenced by the ultrasonication test. The efficacy of the transparent heater for outdoor stability was further demonstrated by continuously operating for many defrosting cycles.

Fig. 5 Temperature vs. time plot of the frost and defrost cycles. Each time V_{ON} of 3 V was applied for nearly 60 s. The cycles were conducted by placing the transparent heater over a LN$_2$ container, such that the heater was constantly bathed in the cold vapors (see photographs and IR images in Fig. S11†). The first cycle was started after 2700 s of placing the panel over LN$_2$ vapors.

Experimental

Fabrication of Ag wire mesh

Commercially available crackle paint (Premium Coatings and Chemicals, India) was used as crackling precursor for these experiments. The crackle precursor was diluted with the diluter (0.65 to 1 g mL^{-1}) to get interconnected crackle network. The glass substrates (1.5 mm thickness) were cleaned with water, acetone and IPA prior to template formation. The crackle precursor was drop coated on the substrates and allowed to spread. The presence of film forming agents (ethyl acetate and pentyl acetate) in crackle precursor enables the spreading and leveling leading to a uniform film coating over large area (*vide infra*). The wet film was allowed to dry under room temperature conditions without any disturbance. Ag metal was physically deposited in the crackle grooves using a resistive thermal evaporator (Hind Hivac, India) at a base pressure of 10^{-6} torr and the template was lifted off neatly by gently rinsing it in acetone resulting in a chemically clean metal network. For surface modification, Ag mesh/glass was dipped in a 10 mM solution of 1-hexadecanethiol in ethanol for overnight.

Characterization

Thickness of the metal network was measured using a Wyko NT9100 Optical Profiling System (Bruker, USA). Scanning electron microscopic (SEM) images were obtained using a Nova NanoSEM 600 instrument (FEI Co., The Netherlands). Energy-dispersive spectroscopy (EDS) analysis of the Ag mesh was performed with an EDAX Genesis instrument (Mahwah, NJ) attached to the SEM column. ImageJ software was used to perform fill factor analysis of the crackle and metal mesh. Transmittance spectra were obtained using a Perkin-Elmer Lambda 900 UV/visible/near-IR spectrophotometer from 400–1300 nm. The resistance was measured using a 4-Point Probe Station (Techno Science Instruments, India). Ultrasonication test was performed using a sonicator (Elmasonic P) at a frequency of 30 kHz and at maximum power. DMM viewer software was used to record the resistance change during ultrasonication test by interfacing a multimeter with a computer. Thermal images were captured using Testo thermal imager (Testo 885). For joule heating the mesh, silver epoxy contacts were made at the two sides of the electrode and thermal images were captured from the backside of the TCE. Later, the images were analyzed using the offline software. The optical images were acquired with the microscope of Laben, India. The weight loss of the crackle precursor, while drying was carried out using a weighing balance from Shimadzu (AUW 220D). The transmittance mapping was performed by scanning the sample with a scanner (hp Scanjet 2400) and intensity distribution was analysed using ImageJ software. XRD measurements were performed on a Miniflex (Rigaku, Japan).

Acknowledgements

References

1 J. Andrey and R. Olley, *Clim. Bull.*, 1990, **24**, 123–136.
2 S. K. Thomas, R. P. Cassoni and C. D. MacArthur, *J. Aircr.*, 1996, **33**, 841–854.
3 J. Laforte, M. Allaire and J. Laflamme, *Atmos. Res.*, 1998, **46**, 143–158.
4 P. Guo, Y. Zheng, M. Wen, C. Song, Y. Lin and L. Jiang, *Adv. Mater.*, 2012, **24**, 2642–2648.
5 X. Chen, R. Ma, H. Zhou, X. Zhou, L. Che, S. Yao and Z. Wang, *Sci. Rep.*, 2013, **3**, 2515.
6 J. Lv, Y. Song, L. Jiang and J. Wang, *ACS Nano*, 2014, **8**, 3152–3169.
7 B. Radha, S. H. Lim, M. S. M. Saifullah and G. U. Kulkarni, *Sci. Rep.*, 2013, **3**, 1078.
8 H. A. Stone, *ACS Nano*, 2012, **6**, 6536–6540.
9 D. S. Hecht, L. Hu and G. Irvin, *Adv. Mater.*, 2011, **23**, 1482–1513.
10 R. Gupta, S. Walia, M. Hösel, J. Jensen, D. Angmo, F. C. Krebs and G. U. Kulkarni, *J. Mater. Chem. A*, 2014, **2**, 10930–10937; R. Gupta and G. U. Kulkarni, *ACS Appl. Mater. Interfaces*, 2013, **5**, 730–736.
11 D. Sui, Y. Huang, L. Huang, J. Liang, Y. Ma and Y. Chen, *Small*, 2011, **7**, 3186–3192.
12 Y. H. Yoon, J. W. Song, D. Kim, J. Kim, J. K. Park, S. K. Oh and C. S. Han, *Adv. Mater.*, 2007, **19**, 4284–4287.
13 J. Ederth, G. A. Niklasson, A. Hultåker, P. Heszler, C. G. Granqvist, A. R. van Doorn, M. J. Jongerius and D. Burgard, *J. Appl. Phys.*, 2003, **93**, 984–988.
14 K. Im, K. Cho, J. Kim and S. Kim, *Thin Solid Films*, 2010, **518**, 3960–3963.
15 K. Im, K. Cho, K. Kwak, J. Kim and S. Kim, *J. Nanosci. Nanotechnol.*, 2013, **13**, 3519–3521.
16 R. Po, C. Carbonera, A. Bernardi, F. Tinti and N. Camaioni, *Sol. Energy Mater. Sol. Cells*, 2012, **100**, 97–114.
17 A. Kumar and C. Zhou, *ACS Nano*, 2010, **4**, 11–14.
18 S. Pang, Y. Hernandez, X. Feng and K. Müllen, *Adv. Mater.*, 2011, **23**, 2779–2795.
19 X. Wang, L. J. Zhi and K. Mullen, *Nano Lett.*, 2008, **8**, 323–327.
20 R. M. Osuna, V. Hernández, J. T. López Navarrete, E. I. Kauppinen and V. Ruiz, *J. Phys. Chem. Lett.*, 2010, **1**, 1367–1371.
21 C. Feng, K. Liu, J.-S. Wu, L. Liu, J.-S. Cheng, Y. Zhang, Y. Sun, Q. Li, S. Fan and K. Jiang, *Adv. Funct. Mater.*, 2010, **20**, 885–891.
22 H. Guo, N. Lin, Y. Chen, Z. Wang, Q. Xie, T. Zheng, N. Gao, S. Li, J. Kang, D. Cai and D.-L. Peng, *Sci. Rep.*, 2013, **3**, 2323.
23 S. De, T. M. Higgins, P. E. Lyons, E. M. Doherty, P. N. Nirmalraj, W. J. Blau, J. J. Boland and J. N. Coleman, *ACS Nano*, 2009, **3**, 1767–1774.
24 M. G. Kang and L. J. Guo, *Adv. Mater.*, 2007, **19**, 1391–1396.
25 M. Vosgueritchian, D. J. Lipomi and Z. Bao, *Adv. Funct. Mater.*, 2012, **22**, 421–428.

26 S. B. Yang, B.-S. Kong, D.-H. Jung, Y.-K. Baek, C.-S. Han, S.-K. Ohe and H.-T. Jung, *Nanoscale*, 2011, **3**, 1361–1373.

27 M.-S. Lee, K. Lee, S.-Y. Kim, H. Lee, J. Park, K.-H. Choi, H.-K. Kim, D.-G. Kim, D.-Y. Lee, S. W. Nam and J.-U. Park, *Nano Lett.*, 2013, **13**, 2814–2821.

28 H. Chang, G. Wang, A. Yang, X. Tao, X. Liu, Y. Shen and Z. Zheng, *Adv. Funct. Mater.*, 2010, **20**, 2893–2902.

29 J. J. Bae, S. C. Lim, G. H. Han, Y. W. Jo, D. L. Doung, E. S. Kim, S. J. Chae, T. Q. Huy, N. Van Luan and Y. H. Lee, *Adv. Funct. Mater.*, 2012, **22**, 4819–4826.

30 J. Kang, H. Kim, K. S. Kim, S.-K. Lee, S. Bae, J.-H. Ahn, Y.-J. Kim, J.-B. Choi and B. H. Hong, *Nano Lett.*, 2011, **11**, 5154–5158.

31 B.-J. Lee and G.-H. Jeong, *Curr. Appl. Phys.*, 2012, **12**, S113–S117.

32 D. Janas, A. Cabrero-Vilatela, J. Bulmer, L. Kurzepa and K. K. Koziol, *Carbon*, 2013, **64**, 305–314.

33 H.-S. Jang, S. K. Jeon and S. H. Nahm, *Carbon*, 2011, **49**, 111–116.

34 D. Jung, D. Kim, K. H. Lee, L. J. Overzet and G. S. Lee, *Sens. Actuators, A*, 2013, **199**, 176–180.

35 T. J. Kang, T. Kim, S. M. Seo, Y. J. Park and Y. H. Kim, *Carbon*, 2011, **49**, 1087–1093.

36 Z. P. Wu and J. N. Wang, *Phys. E*, 2009, **42**, 77–81.

37 T. H. Kim, W. M. Choi, D. H. Kim, M. A. Meitl, E. Menard, H. Jiang, J. A. Carlisle and J. A. Rogers, *Adv. Mater.*, 2008, **20**, 2171–2176.

38 T. Y. Kim, Y. W. Kim, H. S. Lee, H. Kim, W. S. Yang and K. S. Suh, *Adv. Funct. Mater.*, 2013, **23**, 1250–1255.

39 D. Kim, L. Zhu, D.-J. Jeong, K. Chun, Y.-Y. Bang, S.-R. Kim, J.-H. Kim and S.-K. Oh, *Carbon*, 2013, **63**, 530–536.

40 T. Tokuno, M. Nogi, J. Jiu, T. Sugahara and K. Suganuma, *Langmuir*, 2012, **28**, 9298–9302.

41 D. E. Lee, S. J. Go, G. S. Hwang, B. D. Chin and D. H. Lee, *Langmuir*, 2013, **29**, 12259–12265.

42 B. Han, *et al.*, *Adv. Mater.*, 2014, **26**, 873–877.

43 K. D. M. Rao and G. U. Kulkarni, *Nanoscale*, 2014, **6**, 5645–5651.

44 K. D. M. Rao, R. Gupta and G. U. Kulkarni, *Adv. Mater. Interfaces*, 2014, DOI: 10.1002/admi.201400090.

45 S. Kiruthika, R. Gupta, K. D. M. Rao, S. Chakraborty, N. Padmavathy and G. U. Kulkarni, *J. Mater. Chem. C*, 2014, **2**, 2089–2094.

46 S. Kiruthika, K. D. M. Rao, K. Ankush, R. Gupta and G. U. Kulkarni, *Mater. Res. Express.*, 2014, **1**, 026301.

47 M. S. Tirumkudulu and W. B. Russel, *Langmuir*, 2005, **21**, 4938–4948.

48 W. P. Lee and A. F. Routh, *Langmuir*, 2004, **20**, 9885–9888.

49 J. C. Love, L. A. Estroff, J. K. Kriebel, R. G. Nuzzo and G. M. Whitesides, *Chem. Rev.*, 2005, **105**, 1103–1169.

50 J. Wang, Z. Fang, H. Zhu, B. Gao, S. Garner, P. Cimo, Z. Barcikowski, A. Mignerey and L. Hu, *Thin Solid Films*, 2014, **556**, 13–17.

51 S. Wang, X. Zhang and W. Zhao, *J. Nanomater.*, 2013, 456098.

52 X. Zhang, X. Yan, J. Chen and J. Zhao, *Carbon*, 2014, **69**, 437–443.